photonics

MDPI

Type of the Paper (Article)

Light confinement in twisted single-layer 2D+ moiré photonic crystals and bilayer moiré photonic crystals

Steve Kamau [1], Noah Hurley [1], Anupama Kaul[2,3], Jingbiao Cui [1] and Yuankun Lin [1,3,*]

[1] Department of Physics, University of North Texas, Denton, TX 76203, USA; stevekamau@my.unt.edu (S.K.); noahhurley@my.unt.edu (N.H.); Jingbiao.Cui@unt.edu (J.C.)
[2]Department of Materials Science and Engineering, University of North Texas, Denton, TX 76203, USA; Anupama.Kaul@unt.edu (A.K.)
[3] Department of Electrical Engineering, University of North Texas, Denton, TX 76203, USA.
* Correspondence: yuankun.lin@unt.edu; Tel.: +1-940-565-4548

Abstract: Twisted photonic crystals are photonic analogs of twisted monolayer materials such as graphene and their optical property studies are still in their infancy. This paper reports optical properties of twisted single-layer 2D+ moiré photonic crystals where there is weak modulation in z-direction, and bilayer moiré-overlapping-moiré photonic crystals. In weak-coupling bilayer moiré-overlapping-moiré photonic crystals, the light source is less localized with increasing twist angle, similar to the results reported by Harvard's research group in references 37 and 38 in twisted bilayer photonic crystal although there is a gradient pattern in the former case. In a strong-coupling case, however, the light source is tightly localized in AA-stacked region in bilayer PhCs with a large twist angle. For single-layer 2D+ moiré photonic crystals, the light source in Ex polarization can be localized and forms resonance modes when the single-layer 2D+ moiré photonic crystal is integrated on a glass substrate. This study leads toward a potential application of 2D+ moire photonic crystal in future on-chip ~~optoelctronic~~optoelectronic integration.

Keywords: Interference; photonic crystal; twisted bilayer photonic crystal; moiré photonic crystal; resonance mode; micro-nano optics.

1. Introduction

Recent studies of twisted moiré graphene (twistronics) have resulted in numerous exotic phenomena including magic-angle physics and magic-angle flat-band superconductivity [1–6]. Thise explosion of magic-angle physics has advanced from bilayer moiré graphene [7,8] to twisted bilayers of two-dimensional (2D) transition metal dichalcogenide materials [9–12], to recent mixing of moiré-surface and bulk states in graphite [13], and moiré quasicrystals [6]. With increasing moiré periods in length scale, the twistronics for electrons has been advanced to twisted metasurfaces [14–16], and twisted photonic crystals (PhCs) (twistoptics for photons) [17,18]. There are also flat-band modes and magic angles in twisted bilayer PhCs through the mode coupling between two twisted layers [19–25]. Moiré flat-band thresholdless lasing [22] in twistoptics is the optical analogy to superconductivity in twistronics.

Moiré PhCs can be ~~a~~ twisted bilayers [8,18,20,21,23,24,26–38] that can be ideally fabricated by E-beam lithography or twisted single layer moiré pattern [19,22,39–48] that is formed by laser interference in photorefractive crystals, holographic lithography or E-beam lithography. The single layer moiré photonic lattice has been generated in a photorefractive crystal by a shallow modulation of the refractive index induced by two mutually twisted laser interferences, however, both sublattices interfere in one plane [39,40,45]. When four laser beams are arranged in a cone geometry and form an interference pattern,

a conventional PhC can be obtained through holographic lithography. When eight laser beams are separated into two sets with each arranged in different cone angles (where one cone angle is much bigger than the other) in holographic interference geometry, twisted moiré PhCs can be fabricated holographically [49–51]. By including a central laser beam with eight laser beams in cone arrangement, three-dimension (3D) moiré PhCs have been fabricated [52,53].

These single layer moiré PhCs can be easily fabricated by holographic fabrication while the fabrication of bilayer PhCs is rather complicated. Resonance modes have been observed in twisted single-layer moiré PhCs covering Mie-resonances, photonic band edge resonances, and resonance modes above the lightline that might be topological bound states in continuum (BICs), assuming a 2D pattern [17]. Actually, the interference pattern formed by eight beams in two cone geometry is~~are~~ not 2D because there is a weak modulation in z-direction. Here we name them twisted 2D+ moiré PhCs. It is interesting to know whether the light can be confined in these 2D+ moiré PhCs. In this paper, light confinement is studied in two types of twisted PhCs: moiré PhCs superposed against each other with a relative rotation angle (moiré-overlapping-moiré) and single layer 2D+ moiré PhCs. We initially repeat our simulations and compare them with Harvard's results in references 37 and 38. We study the light confinement in 2D+ moiré silicon PhCs with a certain thickness and further on the case where the 2D+ moiré silicon PhCs is on glass substrate.

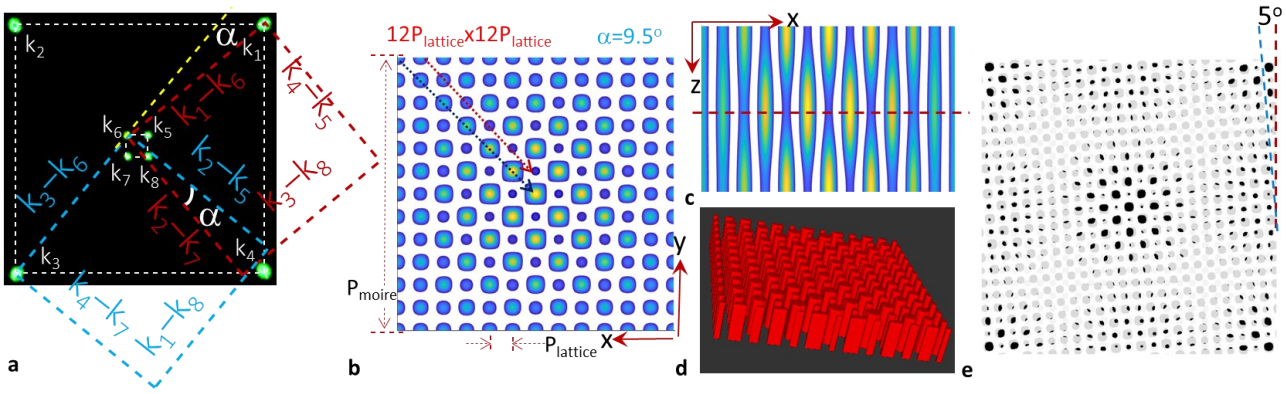

Fig. 1. (a) Photo of eight green laser spots at the Fourier Filter plane and schematic of their wavevectors, wavevector differences and rotation by an angle of α. (b) Twisted moiré pattern from eight beam laser interference in xy plane with a super-cell size of $12P_{lattice} \times 12P_{lattice}$. (c) Eight beam laser interference pattern in xz plane with one period thickness in z-direction. (d) Permittivity structure generated from MEEP simulation for 2D moiré pattern with certaon thickness. (e) The 2D moiré pattern overlapping and rotating by an angle of 5 degrees on another 2D moiré pattern.

2. Concepts and Simulation Methods

The orientation of the interference pattern of two laser beams with wavevectors of k_n and k_m is determined by the wave vector difference k_m-k_n. Two sets of laser beams are shown in Fig. 1a in the Fourier filter of 4f imaging system as green spots. The wavevectors in the xy-plane of four outer beams are labelled as k_1, k_2, k_3 and k_4 while those xy components of four inner beams are k_5, k_6, k_7 and k_8. As shown in Fig. 1a, the wave vector difference (k_3-k_6) is rotated from (k_1-k_6) by an angle of ~~a~~α. The dash blue square formed by ((k_3-k_6), (k_4-k_7), (k_1-k_8) and (k_2-k_5) is rotated from the dash red square of ((k_3-k_8), (k_4-k_5), (k_1-k_6) and (k_2-k_7) by an angle of α~~a~~ too. When all eight beams are overlapped, a moiré interference pattern can be formed as seen in Fig. 1b where the moiré period $P_{moiré}$ and

lattice period $P_{lattice}$ are indicated. The moire interference intensity of these eight beams, I(x,y,z), can be calculated by Eq. (1):

$$I(x,y,z) = \langle \sum_{i=1}^{8} E_i^2(x,y,z,t) \rangle + \sum_{i<j}^{8} E_i E_j e_i \cdot e_j cos\left[\left(k_j - k_i\right) \cdot r + (\delta_j - \delta_i)\right]. \quad (1)$$

where e is the polarization of the electric field, k is the wave vector of laser beams, E is the electric field, and δ is the initial phase. These four outer beams k_1, k_2, k_3 and k_4 ~~determines~~determine the lattice constant $P_{lattice}$. When the interference angles among the four inner beams k_5, k_6, k_7 and k_8 are much smaller than thoese of the four outer beams, k_5, k_6, k_7 and k_8 determine the moire lattice constant P_{moire}. Thus t~~T~~hei~~r~~ relationship of $P_{moiré}$ and $P_{lattice}$ with the twist angle α can be approximately calculated by Eq. (1) [17] below:

$$P_{moire} \cong \frac{P_{lattice}}{\tan\left(\frac{\alpha}{2}\right)} \quad (1)$$

For the interference pattern in the xy plane in Fig. 1b with a unit super-cell size of $12p_{lattice} \times 12p_{lattice}$, the twist angle is calculated to be 9.5 degrees using Eq. (1). There are two sublattices as indicated by the dash blue arrow for motif size increase and dash red arrow for motif size decrease. The interference pattern in the xz plane is shown in Fig. 1c with one z-period. There is a modulation in z-direction, however the modulation is gradient. It is stronger in the central region than at the edge in Fig. 1c. The weak coupling between dual-sub-lattices lead to a disappearance of the first-order diffraction spots of (1, 0), (0, 1), (-1, 0) and (0, -1) as confirmed by experiments [ref].

We generate two ~~type~~types of patterns. One is for conventional twisted PhCs where there is no z-direction modulation in the top or bottom layer PhC separated by a spacer in order to compare our results with Harvard's research group [37, 38]. However, we add moire pattern in the top or bottom layer that is different from Harvard's research group. There are many parameters of top (bottom) layer thickness, spacer thickness, rotation ~~angel~~angle and material permittivity that can modify the light confinement. We start with parameters of top (bottom) layer thickness, spacer thickness, and rotation ~~angels~~angles from Harvard in references 37 and 38 then further evaluate the light confinement related to the thickness and material permittivity. ~~Second~~The second type of pattern maintains the z-direction modulation in Fig. 1c.

We describe the generation of the first type of pattern below. For moiré PhC rotating by an angle of α and overlaying on another moiré PhC, we calculated the interference intensity for xy plane in z-location as indicated by dash red line in Fig. 1c using a Python program. When the intensity of interference = I(x,y,0) is larger than a threshold intensity I_{th} which is 18% of maximum of I(x,y,z) (I_{max}), we assign a refractive index n=3.48, otherwise n=1 (air). In the python program, a certain thickness of pattern was obtained by filling it with the pattern I(x,y,0) as shown in Fig. 1d, an output image of the python simulation. However, for the pattern in Fig. 1e, we assign n=1 if I(x,y,z)>I_{th} otherwise n=3.48 in order to have a clear visual image of moiré patterns.

Because of large unit super-cell used in twisted PhCs, machine learning will be preferred otherwise it is not possible for human force to finish the simulations with many variables. It is better to have simulations in Python language instead of conventional scheme language. We have a detailed material parameter alignment below:

```
def Et(r):
return np.sum(doEside(r),axis=0)
def It(r):
return np.dot(Et(r),np.conj(Et(r)))
```

```
def matfunc1(r):
newvec = np.array([r[0], r[1] , z_slice])
Itnewvec = It(newvec)
if Itnewvec.real > thres:
return mathigh
else:
return matlow
```

Where we have matlow=square of 1 and mathigh=square of 3.48 in our simulations in Fig. 2.

For the generation of the second type of pattern for single layer 2D+ moiré PhCs, we assign the interference intensity I (x,y,z) to p-type silicon [54] in Fig. 1c when $I_{th}>I_{max}$ otherwise to air (n=1). In the simulation, we setup a basis of 1 μm for the lattice constant $P_{lattice}$ (a in the simulation program). A super-cell of 24 $P_{lattice}$×24 $P_{lattice}$ is used for one layer PhC. ~~Actually~~Actually, the simulation is scalable with the parameter a. If the frequency f=a/λ=0.3, we can change the parameter a based on the wavelength of interest. The permittivity of p-type silicon in the simulation program is also scalable with the parameter a. We use the Drude-model in Eq. (2) for p-type silicon: —

$$\varepsilon(\omega) = \varepsilon_b - \frac{\omega_p^2}{\omega^2 + i\Gamma_p\omega} \quad (2)$$

where the background permittivity $\varepsilon_b = 11.7$, the plasma frequency $\omega_p = 0.47$ eV, the carrier relaxation rate $\Gamma_p = 0.095$ eV. We convert these parameters usable for MEEP codes from eV to angular frequency ω and by normalizing them to MEEP units, divided by ωλ/a. In the Python program, we setup scalable permittivity below:

```
# pSi
Si_eps_inf = 11.7
Si_frq = 1e-20
Si_gam = 0.076622725*a
Si_sig = ((0.379080721*a)**2)/(Si_frq**2)
pSi_susc=[mp.DrudeSusceptibility(frequency=Si_frq,gamma=Si_gam,sigma=Si_sig)]
pSi = mp.Medium(epsilon=Si_eps_inf, E_susceptibilities=pSi_susc)
```

Thus the material of rod-type structure is p-type silicon or n=1 while the hole is aire with n=1.

A gaussian source is placed in middle of simulation cell whose size spans the xy dimensions of the photonic crystal. The width of the source (Δ~~d~~f) is broadband. We set Δ~~d~~f = fmax-fmin where fmax and fmin are the maximum frequency and minimum frequency respectively. We set the source to be broadband to study the light confinement while df=0.002 was used for the study of resonance modes [17]. To collect the output, we take either a vertical (zy) or horizontal (xy) slice through the center of the simulation cell and output the E-field intensity on that plane. The simulation code was written in python and made use of the program MEEP [55], which is a finite-difference time-domain (FDTD) simulation software package developed at MIT to model electromagnetic systems. The code was run using Amazon's web servers on the AWS platform. The quality factor (Q-factor) of in resonance modes was calculated using the harmonic inversion function that was included in the MIT MEEP. The runtime for each simulation was in general around 45 minutes.

3. Results of light confinement in bilayer moiré-over-moiré PhC

The bilayer moiré-over-moiré PhCs in Fig. 2 (a1, b1 and c1) are designed following Harvard group's design [37, 38]: top moiré PhC has a thickness=180 nm with a refractive

index contrast of 3.48/1; the coupler (spacer) between two moiré PhCs has a thickness=36 nm for a strong coupling and n=1.48 for polymethyl methacrylate (PMMA) [38]; the bottom moiré PhC has the same structural and material parameters as the top one but is rotated by twist angles of 1.89, 2.13 and 2.88 degrees in Fig. 2 (a1, b1, and c1), respectively. When a light source with both E_x and E_y polarization was used, there was a coupling between top and bottom layers of PhCs for E_y polarization. In this study, we set a light source in an E_y polarization. The light is confined in AA stacked region, similar to Harvard group's results. When the twist angle increases from 1.89 to 2.13 and 2.88 degrees, the AA-stacked region becomes smaller thus it is reasonable to see that the light is confined to a smaller region in Fig. 2(b1) and mostly localized in Fig. 2(c1).

We also calculate the E-field in the xy plane in twisted bilayer moiré-over-moiré PhCs for a weak coupling case where the top and bottom moiré layer thickness=220 nm and the spacer thickness=250 nm[37], for different twist angles of 1.89, 2.13 and 2.88 degrees in Fig. 2(a2, b2, and c2), respectively. Similar to Harvard group's result, the light becomes less localized from the twist angles of 1.89, to 2.13, to 2.88 degrees [37]. In Fig. 2(c2), the light appears outside the AA-stacked region and travels in direction of lattice orientation of top moiré layer which is 2.88 degrees away from y-axis as indicated in the figure. The cross-section view of E-field intensity in yz-plane in Fig. 2d shows a coupling of light in AA-stacked region and light propagation in top moiré layer. The weak coupling of E-fields between dual-sub-lattices is also observed as the blue colors concentrated in one set of lattices in Fig. 2d.

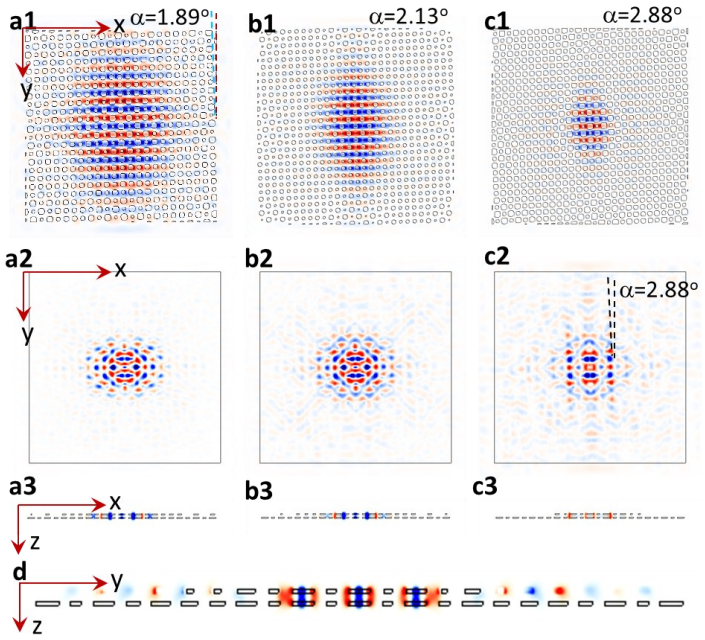

Fig. 2. The twist angle for bilayer moiré PhCs is 1.89, 2.13 and 2.88 degrees for figures in column I, II and III, respectively. (0, 0, *z*), (*x*, 0, 0) or (0, *y*, 0) is at center of each figure. (a1, b1, c1) E-field intensity xy-plane in twisted bilayer moiré-over-moiré PhC where the thicness of top moiré layer, spacer and bottom moiré layer is 180, 36 and 180 nm, respectively. (a2, b2, c2) E-field intensity xy-plane in twisted bilayer moiré-over-moiré PhC with layer thicknesses of 220, 250 and 220 nm, respectively. (a3, b3 and c3) E-field intensity xz-plane as viewed along y=0 in twisted bilayer moiré-over-moiré PhC in (a2, b2 and c2), respectively.(d) E-field intensity yz-plane as viewed along x=0 in (c2).

Besides ~~above~~the above simulations with structural parameters and twist angles from Harvard's research group [37, 38], we perform more simulations on the relationship

between the light confinement and spacer thickness. Starting from the structural parameters in Fig. 2a2 with (220, 250, 220) nm for the thickness of (top layer, spacer, bottom layer), we change the spacer thickness to be 200, 150, and 100 nm. The twist angle is still 1.89 degrees. Fig. 3 shows the simulation results. With the thickness of 200 nm, the light is confined inside the region as indicated by a rectangle in Fig. 3a, similar to the results in Fig. 2a2. There is no big change in Fig. 3b when the spacer thickness is ~~decreased~~decreased to 150 nm. However, the light confinement is very weak in Fig. 3c when the spacer thickness is 100 nm. We can see that E-field distribution looks like a dumbbell shape. With a small spacer thickness, the light confinement in the spacer is competing with those in AA region. It can lead to an application of reconfigurable light confinement or cavity for nanophotonics by a tunable thickness or refractive index of the spacer.

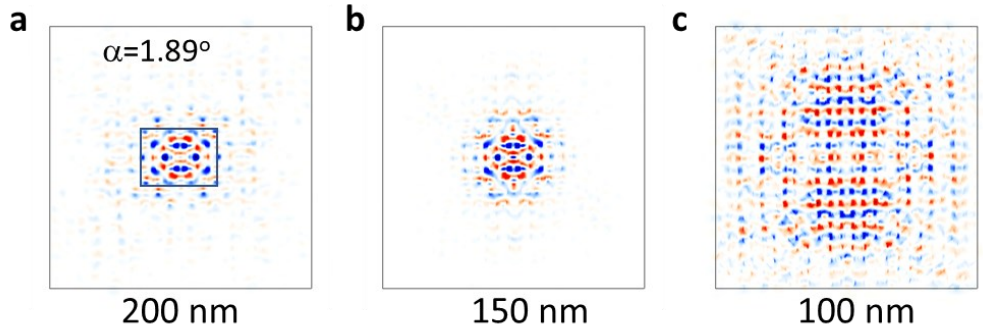

Fig. 3. (a, b, c) E-field intensity in xy-plane in twisted bilayer moiré-over-moiré PhC with layer thicknesses of (220, spacer, 220 nm) where spacer=200 nm (a), 150 nm (b) and 100 nm (c), respectively. The twist angle for bilayer moiré PhCs is 1.89 degrees for all figures. (0,0,z) is at center of each figure.

Now we keep the same layer thickness and twist angle of 1.89 degrees as those in Fig. 2a2, however, change the material property from n=3.48 for rod-type motif to a real p-type silicon for top and bottom layers. Fig. 4a shows E-field intensity in xy-plane in twisted bilayer moiré-over-moiré PhC with layer thicknesses of (220, 250, 220 nm) at times of 8/24 (a1) and 16/24 (a2) period when E-field intensity switches color from red-blue (a1) to blue-red (a2). There are more modes confined inside or outside the rectangle in Fig. 4a1 than those in Fig. 3a and Fig. 2a2 (rectangle is not drawn and mode numbers are compared). It seems the real silicon has a dispersion that can meet the requirement of resonance condition for more modes.

We assume that a small thickness of~~in~~ the spacer relative to that in top or bottom layer in Fig. 2a1 and Fig. 3c leads toward a weak light confinement. We increase the thickness to 455 nm for ~~top~~the top and bottom layers, keep the same thickness of 36 nm for the spacer and change the change the material property from n=3.48 for rod-type motif to a real p-type silicon for top and bottom layers. Fig. 4b1 and 4b2 show E-field intensity in xz-plane in twisted bilayer moiré-over-moiré PhC at times of 1/24 (b1) and 9/24 (b2) of one period, respectively. Fig. 4c shows E-field intensity in yz-plane in the same structure as (b). With a big thickness of top and bottom layers, the light is confined in the middle of structure. The thickness of 455 nm for the top layer+ 455 nm for the bottom layer is close to ~~the half~~half of the z-modulation period in Fig. 1c. The fabrication of twisted PhCs has used a complex process of E-beam lithography patterning, SU-8 based suspending, spacing and bonding. Instead of further study of multi-layer moiré-over-moiré PhCs, we turn to a single layer 2D+ moiré silicon PhC in next section. Furthermore, the bilayer moire PhCs may not easy to be directly integrated in a nanophotonic device, however, single

layer 2D+ moiré silicon PhC is as easy as conventional PhCs for nanophotonics integration. A very-recent publication [56] in reconfigurable moire laser further stimulates such ~~a researchr~~research.

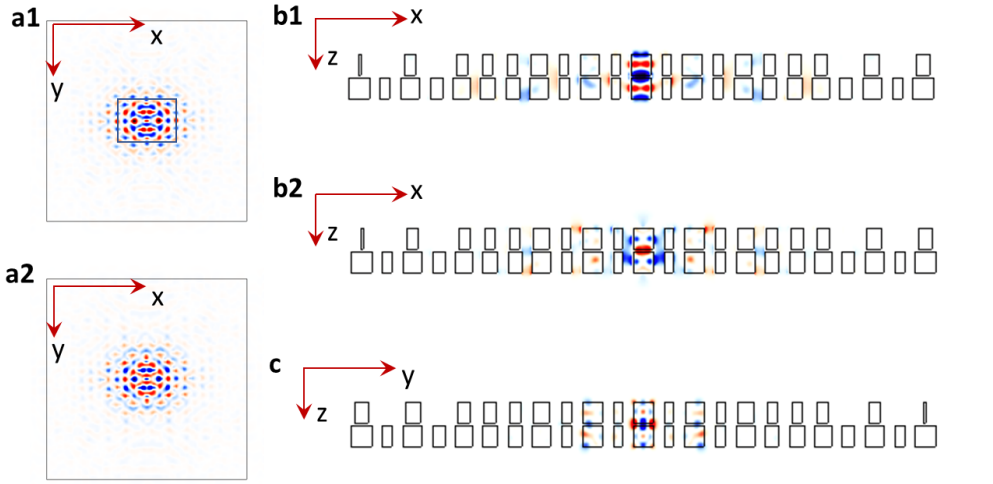

Fig. 4. (a) E-field intensity in xy-plane in twisted bilayer moiré-over-moiré PhC with layer thicknesses of (220, 250, 220 nm) for top layer, spacer and bottom layer at times of 8/24 (a1) and 16/24 (a2) of one period. The twist angle for bilayer moiré PhCs is 1.89 degrees. (0,0,z) is at center of each figure. (b) E-field intensity in xz-plane in twisted bilayer moiré-over-moiré PhC with layer thicknesses of (455, 36, 455 nm) for top layer, spacer and bottom layer at times of 1/24 (b1) and 9/24 (b2) of one period. (c) E-field intensity in yz-plane in the same structure as (b). The twist angle for bilayer moiré PhCs is 1.89 degrees. (0, 0, z) (a), (0, y, 0) (b) or (x, 0, 0) (c) is at center of each figure.

4. Results of light confinement in 2D+ moiré silicon PhCs

The fabrication of single layer 2D+ moiré silicon can start from a thick photoresist of SU-8 instead of Dipentaerythritol penta-/hexa-acrylate (DPHPA) used recently for 3D moire PhCs [52,53]. The eight-beam interference pattern can be recorded in ~~thick photoresist, such as~~ SU-8 that can be~~,~~ post-exposure baked and developed. The developed PhCs in SU-8 can be filled with SiO2 then burn away SU-8. Then PhCs in SiO2 can be filled with silicone and SiO2 is etched away~~and~~ (a double-conversion process)~~ted into silicon~~. We set the thickness of 2D+ moiré silicon PhCs to be half~~0.5~~ of the z-modulation period. The simulated E-field intensity has been output into 20 images at the (1/20), (2/20), (3/20) … (20/20) step of the time-period. ~~Fig. 3~~Fig. 5(a,b) show the E-field intensity in 2D+ moiré silicon PhCs in two of above moments when their intensities are switched, i.e. the blue color becomes red while the red color becomes blue. In the central regions, the motif in single-layer moiré PhC looks like alternative concave and convex lens. As indicated by the dash red line, the light in Ex polarization is converged into a point as they travel from the central region to the left in ~~Fig. 3~~Fig. 5(a,b). In ~~Fig. 3~~Fig. 5(c,d), the red color switches with blue color and the light source in Ex polarization is also converged as indicated by the dash red line. ~~Fig. 3~~Fig. 5(e,f) show E-field intensity in zy-plane in twisted single-layer moiré PhC with a thickness equal to half~~=0.5~~the z-modulation period in pairs that switch E-field strength in E_z polarization during oscillations. They look like a standing wave with

top and bottom edges as boundaries. If the single-layer moiré PhCs are fabricated on a substrate, these modes will radiate into the substrate and air as shown below.

~~Fig. 3~~Fig. 5(g,h) show E-field intensity in the zy-plane for polarization E_x and E_z respectively, ~~–~~in twisted single-layer moiré PhC with a thickness equal to ~~=~~half the~~0.5~~ z-modulation period on 500 nm glass substrate. The oscillation modes in both figures maintain a mirror symmetry along y=0, however, don't have a mirror symmetry along z=0 as expected. It is clearly observed that the light source in E_x polarization is localized in the single-layer moiré PhCs, however, the localization cannot sustain for E_z polarization in ~~Fig. 3~~Fig. 5h.

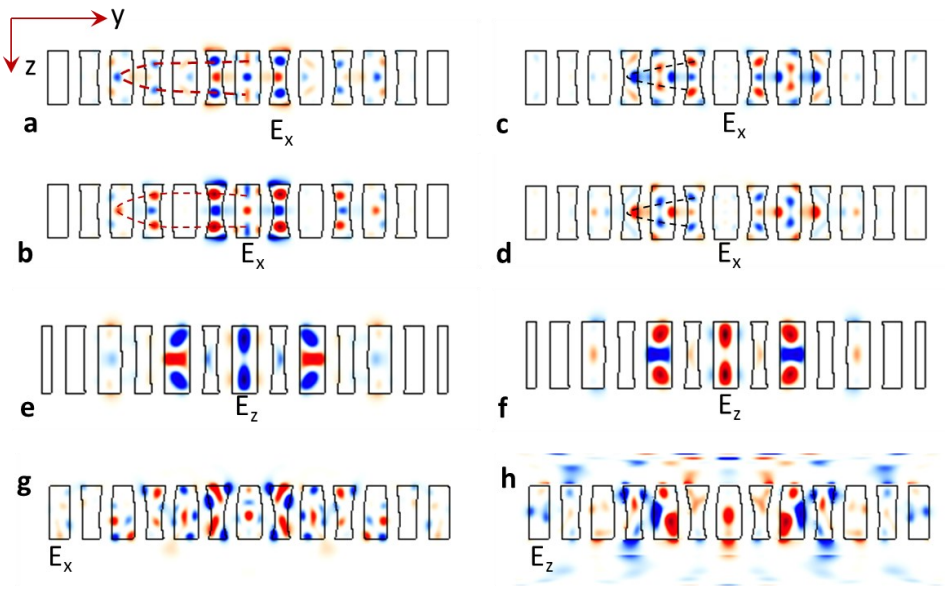

~~Fig. 3~~Fig. 5. E-field intensity in zy-plane in twisted single-layer 2D+ moiré PhC with a thickness=0.5 z-modulation period in pairs that switch E-field strength in E_x polarization during oscillations in (a,b) and (c,d) and pairs that switch E-field strength in E_z polarization during oscillations in (e,f). (g,h) E-field intensity in zy-plane for polarization E_x (g) and E_z (h) in twisted single-layer 2D+ moiré PhC with a thickness=0.5 z-modulation period on 500 nm glass substrate.

5. Discussion

In the simulation, we have used a resolution of 24 (relatively low) due to the large 3D unit super-cell size. In both fabrications and simulations, a thin single-layer moiré PhC is favored. Although the simulation of resonance modes and calculation of their Q-factors were not in high resolutions, we observed a trend of increasing Q-factors with an increasing thickness of single-layer moiré PhCs. The maximum Q-factor for resonance modes with Ex polarization is in the magnitude order of 10^3 for single-layer moiré PhCs with a thickness of 0.5 z-modulation period while it is the order of 10^4 when the thickness is one z-modulation period. As shown in ~~Fig. 4~~Fig. 6(a,b,c) for E-field intensity in the xy-plane and zy-plane, respectively, for polarization E_x in twisted single-layer 2D+ moiré PhC with a thickness of one z-modulation period. Although it is a relatively ~~low resolution~~low-resolution simulation, resonance modes are clearly visible and symmetric. As expected, the E-field is propagating along the same set of sub-lattices. In zy plane in ~~Fig. 4~~Fig. 6(b,c), the resonance mode is not a standing wave in z-direction and can survive when the single-layer 2D+ moiré PhCs are fabricated on a glass substrate.

The validation of simulation results is necessary as did in recent application [56]. The simulated E-field propagation along the same set of sub-lattices in Fig. 5(a , b, e) corresponds to the disappearance of first order diffraction spots that have recently been observed in experiments [48]. Next step we should work on the fabrication of the single-layer 2D+ moiré PhCs in silicone through the double-conversion process described above. For the single-layer moire PhCs in active medium for lasing application, it can be realized by integrating 2D layered materials on PhCs.

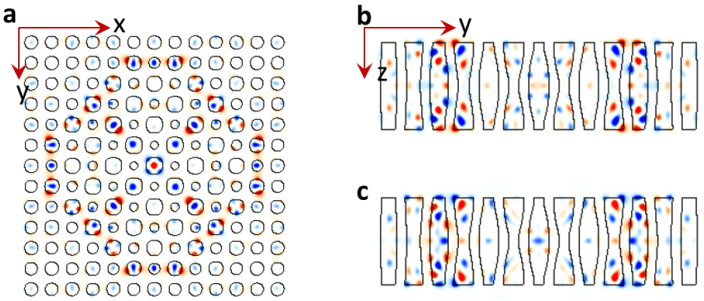

~~Fig. 4~~Fig. 6. (a) E-field intensity with E_x polarization in xy-plane in twisted single-layer 2D+ moiré PhC with a thickness=one z-modulation period. (b,c) E-field intensity with E_x polarization in zy-plane in twisted single-layer 2D+ moiré PhC with a thickness of one z-modulation period in pairs that switch E-field strength.

6. Conclusion

We have studied light confinement in bilayer twisted moiré-overlapping-moiré PhCs and single-layer 2D+ moiré PhCs. In weakly-coupled moiré-overlapping-moiré PhCs, the light source is less localized with increasing twist angle while the light source is tightly localized with increasing twist angle in the strong coupling case. For the single-layer 2D+ moiré PhCs, the light source with E_z polarization cannot survive when the PhCs are integrated on a glass substrate. Lens effects and resonance modes are observed for the light source with E_x polarization in single-layer 2D+ moiré PhCs. The most importantly, we conclude that the single-layer 2D+ moiré PhCs is very promising and ready for an integration in nanophotonic devices.

Author Contributions: Conceptualization, Y. L., J.C., and A.K.; methodology, S.K., N.H.,Y.L., and J.C.,; software, S.K., N.H. and Y.L.; investigation, S.K., N.H. and Y.L; formal analysis, Y.L.,and S.K.; writing—original draft preparation, S.K. and Y.L.; writing—review and editing, All; funding acquisition, A.K., J.C. and Y.L. All authors have read and agreed to the published version of the manuscript.

Funding: This research was partially supported by the U.S. National Science Foundation, grant number 2128367 and by the Department of Energy/National Nuclear Security Administration under Award Number DE-NA0004114. This report was prepared as an account of work sponsored by an agency of the United States Government. Neither the United States Government nor any agency thereof, nor any of their employees, makes any warranty, express or implied, or assumes any legal liability or responsibility for the accuracy, completeness, or usefulness of any information, apparatus, product, or process disclosed, or represents that its use would not infringe privately owned rights. Reference herein to any specific commercial product, process, or service by trade name, trademark, manufacturer, or otherwise does not necessarily constitute or imply its endorsement, recommendation, or favoring by the United States Government or any agency thereof. The views and opinions of authors expressed herein do not necessarily state or reflect those of the United States Government or any agency thereof.

Conflicts of Interest: The authors declare no conflict of interest.

Data Availability Statement: Data will be available upon request.

References

1. Cao, Y.; Fatemi, V.; Fang, S.; Watanabe, K.; Taniguchi, T.; Kaxiras, E.; Jarillo-Herrero, P. Unconventional Superconductivity in Magic-Angle Graphene Superlattices. *Nature* **2018**, *556*, 43–50, doi:10.1038/nature26160.
2. Yankowitz, M.; Chen, S.; Polshyn, H.; Zhang, Y.; Watanabe, K.; Taniguchi, T.; Graf, D.; Young, A.F.; Dean, C.R. Tuning Superconductivity in Twisted Bilayer Graphene. *Science (1979)* **2019**, *363*, 1059–1064, doi:10.1126/science.aav1910.
3. Balents, L.; Dean, C.R.; Efetov, D.K.; Young, A.F. Superconductivity and Strong Correlations in Moiré Flat Bands. *Nat Phys* **2020**, *16*, 725–733, doi:10.1038/s41567-020-0906-9.
4. Arora, H.S.; Polski, R.; Zhang, Y.; Thomson, A.; Choi, Y.; Kim, H.; Lin, Z.; Wilson, I.Z.; Xu, X.; Chu, J.-H.; et al. Superconductivity in Metallic Twisted Bilayer Graphene Stabilized by WSe2. *Nature* **2020**, *583*, 379–384, doi:10.1038/s41586-020-2473-8.
5. González, J.; Stauber, T. Kohn-Luttinger Superconductivity in Twisted Bilayer Graphene. *Phys Rev Lett* **2019**, *122*, 026801, doi:10.1103/PhysRevLett.122.026801.
6. Uri, A.; de la Barrera, S.C.; Randeria, M.T.; Rodan-Legrain, D.; Devakul, T.; Crowley, P.J.D.; Paul, N.; Watanabe, K.; Taniguchi, T.; Lifshitz, R.; et al. Superconductivity and Strong Interactions in a Tunable Moiré Quasicrystal. *Nature* **2023**, *620*, 762–767, doi:10.1038/s41586-023-06294-z.
7. Uchida, K.; Furuya, S.; Iwata, J.-I.; Oshiyama, A. Atomic Corrugation and Electron Localization Due to Moiré Patterns in Twisted Bilayer Graphenes. *Phys Rev B* **2014**, *90*, 155451, doi:10.1103/PhysRevB.90.155451.
8. Sunku, S.S.; Ni, G.X.; Jiang, B.Y.; Yoo, H.; Sternbach, A.; McLeod, A.S.; Stauber, T.; Xiong, L.; Taniguchi, T.; Watanabe, K.; et al. Photonic Crystals for Nano-Light in Moiré Graphene Superlattices. *Science (1979)* **2018**, *362*, 1153–1156, doi:10.1126/science.aau5144.
9. Wu, F.; Lovorn, T.; Tutuc, E.; Martin, I.; MacDonald, A.H. Topological Insulators in Twisted Transition Metal Dichalcogenide Homobilayers. *Phys Rev Lett* **2019**, *122*, 086402, doi:10.1103/PhysRevLett.122.086402.
10. Bai, Y.; Zhou, L.; Wang, J.; Wu, W.; McGilly, L.J.; Halbertal, D.; Lo, C.F.B.; Liu, F.; Ardelean, J.; Rivera, P.; et al. Excitons in Strain-Induced One-Dimensional Moiré Potentials at Transition Metal Dichalcogenide Heterojunctions. *Nat Mater* **2020**, *19*, 1068–1073, doi:10.1038/s41563-020-0730-8.
11. Zhang, Z.; Wang, Y.; Watanabe, K.; Taniguchi, T.; Ueno, K.; Tutuc, E.; LeRoy, B.J. Flat Bands in Twisted Bilayer Transition Metal Dichalcogenides. *Nat Phys* **2020**, *16*, 1093–1096, doi:10.1038/s41567-020-0958-x.
12. Naik, M.H.; Jain, M. Ultraflatbands and Shear Solitons in Moiré Patterns of Twisted Bilayer Transition Metal Dichalcogenides. *Phys Rev Lett* **2018**, *121*, 266401, doi:10.1103/PhysRevLett.121.266401.
13. Mullan, C.; Slizovskiy, S.; Yin, J.; Wang, Z.; Yang, Q.; Xu, S.; Yang, Y.; Piot, B.A.; Hu, S.; Taniguchi, T.; et al. Mixing of Moiré-Surface and Bulk States in Graphite. *Nature* **2023**, *620*, 756–761, doi:10.1038/s41586-023-06264-5.
14. Liu, S.; Ma, S.; Shao, R.; Zhang, L.; Yan, T.; Ma, Q.; Zhang, S.; Cui, T.J. Moiré Metasurfaces for Dynamic Beamforming. *Sci Adv* **2022**, *8*, eabo1511, doi:10.1126/sciadv.abo1511.

15. Hu, G.; Wang, M.; Mazor, Y.; Qiu, C.-W.; Alù, A. Tailoring Light with Layered and Moiré Metasurfaces. *Trends Chem* **2021**, *3*, 342–358, doi:10.1016/j.trechm.2021.02.004.
16. Hu, G.; Krasnok, A.; Mazor, Y.; Qiu, C.-W.; Alù, A. Moiré Hyperbolic Metasurfaces. *Nano Lett* **2020**, *20*, 3217–3224, doi:10.1021/acs.nanolett.9b05319.
17. Alnasser, K.; Kamau, S.; Hurley, N.; Cui, J.; Lin, Y. Resonance Modes in Moiré Photonic Patterns for Twistoptics. *OSA Contin* **2021**, *4*, 1339, doi:10.1364/OSAC.420912.
18. Duan, J.; Capote-Robayna, N.; Taboada-Gutiérrez, J.; Álvarez-Pérez, G.; Prieto, I.; Martín-Sánchez, J.; Nikitin, A.Y.; Alonso-González, P. Twisted Nano-Optics: Manipulating Light at the Nanoscale with Twisted Phonon Polaritonic Slabs. *Nano Lett* **2020**, *20*, 5323–5329, doi:10.1021/acs.nanolett.0c01673.
19. Lin, H.-M.; Lu, Y.-H.; Chang, Y.-J.; Yang, Y.-Y.; Jin, X.-M. Direct Observation of a Localized Flat-Band State in a Mapped Moiré Hubbard Photonic Lattice. *Phys Rev Appl* **2022**, *18*, 054012, doi:10.1103/PhysRevApplied.18.054012.
20. Dong, K.; Zhang, T.; Li, J.; Wang, Q.; Yang, F.; Rho, Y.; Wang, D.; Grigoropoulos, C.P.; Wu, J.; Yao, J. Flat Bands in Magic-Angle Bilayer Photonic Crystals at Small Twists. *Phys Rev Lett* **2021**, *126*, 223601, doi:10.1103/PhysRevLett.126.223601.
21. Yi, C.-H.; Park, H.C.; Park, M.J. Strong Interlayer Coupling and Stable Topological Flat Bands in Twisted Bilayer Photonic Moiré Superlattices. *Light Sci Appl* **2022**, *11*, 289, doi:10.1038/s41377-022-00977-4.
22. Mao, X.-R.; Shao, Z.-K.; Luan, H.-Y.; Wang, S.-L.; Ma, R.-M. Magic-Angle Lasers in Nanostructured Moiré Superlattice. *Nat Nanotechnol* **2021**, *16*, 1099–1105, doi:10.1038/s41565-021-00956-7.
23. Nguyen, D.X.; Letartre, X.; Drouard, E.; Viktorovitch, P.; Nguyen, H.C.; Nguyen, H.S. Magic Configurations in Moiré Superlattice of Bilayer Photonic Crystals: Almost-Perfect Flatbands and Unconventional Localization. *Phys Rev Res* **2022**, *4*, L032031, doi:10.1103/PhysRevResearch.4.L032031.
24. Wang, H.; Ma, S.; Zhang, S.; Lei, D. Intrinsic Superflat Bands in General Twisted Bilayer Systems. *Light Sci Appl* **2022**, *11*, 159, doi:10.1038/s41377-022-00838-0.
25. Zhou, J.; Xie, S.; Nie, C.; Xu, P.; Yi, J.; Liu, E. Optical Properties of a Moiré-Lattice Photonic Crystal Fiber with Controllable Magic Angle. *Results Phys* **2023**, *51*, 106659, doi:10.1016/j.rinp.2023.106659.
26. Tang, H.; Lou, B.; Du, F.; Zhang, M.; Ni, X.; Xu, W.; Jin, R.; Fan, S.; Mazur, E. Experimental Probe of Twist Angle–Dependent Band Structure of on-Chip Optical Bilayer Photonic Crystal. *Sci Adv* **2023**, *9*, eadh8498, doi:10.1126/sciadv.adh8498.
27. Lou, B.; Wang, B.; Rodríguez, J.A.; Cappelli, M.; Fan, S. Tunable Guided Resonance in Twisted Bilayer Photonic Crystal. *Sci Adv* **2022**, *8*, eadd4339, doi:10.1126/sciadv.add4339.
28. Lou, B.; Zhao, N.; Minkov, M.; Guo, C.; Orenstein, M.; Fan, S. Theory for Twisted Bilayer Photonic Crystal Slabs. *Phys Rev Lett* **2021**, *126*, 136101, doi:10.1103/PhysRevLett.126.136101.
29. Huang, L.; Zhang, W.; Zhang, X. Moiré Quasibound States in the Continuum. *Phys Rev Lett* **2022**, *128*, 253901, doi:10.1103/PhysRevLett.128.253901.
30. Hu, G.; Zheng, C.; Ni, J.; Qiu, C.-W.; Alù, A. Enhanced Light-Matter Interactions at Photonic Magic-Angle Topological Transitions. *Appl Phys Lett* **2021**, *118*, 211101, doi:10.1063/5.0052580.
31. Krasnok, A.; Alù, A. Low-Symmetry Nanophotonics. *ACS Photonics* **2022**, *9*, 2–24, doi:10.1021/acsphotonics.1c00968.

32. Chen, J.; Lin, X.; Chen, M.; Low, T.; Chen, H.; Dai, S. A Perspective of Twisted Photonic Structures. *Appl Phys Lett* **2021**, *119*, 240501, doi:10.1063/5.0070163.
33. Wu, Z.; Zheng, Y. Moiré Chiral Metamaterials. *Adv Opt Mater* **2017**, *5*, 1700034, doi:10.1002/adom.201700034.
34. Lou, B.; Wang, B.; Rodríguez, J.A.; Cappelli, M.; Fan, S. Tunable Guided Resonance in Twisted Bilayer Photonic Crystal. *Sci Adv* **2022**, *8*, eadd4339, doi:10.1126/sciadv.add4339.
35. Zhang, T.; Dong, K.; Li, J.; Meng, F.; Li, J.; Munagavalasa, S.; Grigoropoulos, C.P.; Wu, J.; Yao, J. Twisted Moiré Photonic Crystal Enabled Optical Vortex Generation through Bound States in the Continuum. *Nat Commun* **2023**, *14*, 6014, doi:10.1038/s41467-023-41068-1.
36. Tang, H.; Ni, X.; Du, F.; Srikrishna, V.; Mazur, E. On-Chip Light Trapping in Bilayer Moiré Photonic Crystal Slabs. *Appl Phys Lett* **2022**, *121*, 231702, doi:10.1063/5.0105365.
37. Tang, H.; Du, F.; Carr, S.; DeVault, C.; Mello, O.; Mazur, E. Modeling the Optical Properties of Twisted Bilayer Photonic Crystals. *Light Sci Appl* **2021**, *10*, 157, doi:10.1038/s41377-021-00601-x.
38. Tang, H.; Ni, X.; Du, F.; Srikrishna, V.; Mazur, E. On-Chip Light Trapping in Bilayer Moiré Photonic Crystal Slabs. *Appl Phys Lett* **2022**, *121*, 231702, doi:10.1063/5.0105365.
39. Zeng, J.; Hu, Y.; Zhang, X.; Fu, S.; Yin, H.; Li, Z.; Chen, Z. Localization-to-Delocalization Transition of Light in Frequency-Tuned Photonic Moiré Lattices. *Opt Express* **2021**, *29*, 25388, doi:10.1364/OE.434281.
40. Fu, Q.; Wang, P.; Huang, C.; Kartashov, Y. V.; Torner, L.; Konotop, V. V.; Ye, F. Optical Soliton Formation Controlled by Angle Twisting in Photonic Moiré Lattices. *Nat Photonics* **2020**, *14*, 663–668, doi:10.1038/s41566-020-0679-9.
41. Talukdar, T.H.; Hardison, A.L.; Ryckman, J.D. Moiré Effects in Silicon Photonic Nanowires. *ACS Photonics* **2022**, *9*, 1286–1294, doi:10.1021/acsphotonics.1c01800.
42. Zhou, X.; Lin, Z.; Lu, W.; Lai, Y.; Hou, B.; Jiang, J. Twisted Quadrupole Topological Photonic Crystals. *Laser Photon Rev* **2020**, *14*, 2000010, doi:10.1002/lpor.202000010.
43. Shang, C.; Lu, C.; Tang, S.; Gao, Y.; Wen, Z. Generation of Gradient Photonic Moiré Lattice Fields. *Opt Express* **2021**, *29*, 29116, doi:10.1364/OE.434935.
44. Han, J.-H.; Kim, I.; Ryu, J.-W.; Kim, J.; Cho, J.-H.; Yim, G.-S.; Park, H.-S.; Min, B.; Choi, M. Rotationally Reconfigurable Metamaterials Based on Moiré Phenomenon. *Opt Express* **2015**, *23*, 17443, doi:10.1364/OE.23.017443.
45. Wang, P.; Zheng, Y.; Chen, X.; Huang, C.; Kartashov, Y. V.; Torner, L.; Konotop, V. V.; Ye, F. Localization and Delocalization of Light in Photonic Moiré Lattices. *Nature* **2020**, *577*, 42–46, doi:10.1038/s41586-019-1851-6.
46. Kartashov, Y. V.; Ye, F.; Konotop, V. V.; Torner, L. Multifrequency Solitons in Commensurate-Incommensurate Photonic Moiré Lattices. *Phys Rev Lett* **2021**, *127*, 163902, doi:10.1103/PhysRevLett.127.163902.
47. Khurgin, J.B. Light Slowing down in Moiré Fiber Gratings and Its Implications for Nonlinear Optics. *Phys Rev A (Coll Park)* **2000**, *62*, 013821, doi:10.1103/PhysRevA.62.013821.
48. Khadijah Alnasser, Shan Li, Siraj Sidhik, Steve Kamau, Jin Hou, Noah Hurley, Ayman Alzaid, Sicheng Wang, Hao Yan, Jiangdong Deng, Mohammad A Omary, Aditya D Mohite, Jingbiao Cui and Yuankun Lin. Fabrication of Twisted Moire Photonic Crystal and Random Moire Photonic Crystal and Their Potential Applications in Light Extraction. *Nanotechnology* 2024, *35*, 025203. Doi**:** 10.1088/1361-6528/ad024a

49. Lowell, D.; Lutkenhaus, J.; George, D.; Philipose, U.; Chen, B.; Lin, Y. Simultaneous Direct Holographic Fabrication of Photonic Cavity and Graded Photonic Lattice with Dual Periodicity, Dual Basis, and Dual Symmetry. *Opt Express* **2017**, *25*, 14444, doi:10.1364/OE.25.014444.
50. Lowell, D.; Hassan, S.; Adewole, M.; Philipose, U.; Chen, B.; Lin, Y. Holographic Fabrication of Graded Photonic Super-Crystals Using an Integrated Spatial Light Modulator and Reflective Optical Element Laser Projection System. *Appl Opt* **2017**, *56*, 9888, doi:10.1364/AO.56.009888.
51. Ohlinger, K.; Lutkenhaus, J.; Arigong, B.; Zhang, H.; Lin, Y. Spatially Addressable Design of Gradient Index Structures through Spatial Light Modulator Based Holographic Lithography. *J Appl Phys* **2013**, *114*, 213102, doi:10.1063/1.4837635.
52. Hurley, N.; Kamau, S.; Alnasser, K.; Philipose, U.; Cui, J.; Lin, Y. Laser Diffraction Zones and Spots from Three-Dimensional Graded Photonic Super-Crystals and Moiré Photonic Crystals. *Photonics* **2022**, *9*, 395, doi:10.3390/photonics9060395.
53. Hurley, N.; Kamau, S.; Cui, J.; Lin, Y. Holographic Fabrication of 3D Moiré Photonic Crystals Using Circularly Polarized Laser Beams and a Spatial Light Modulator. *Micromachines (Basel)* **2023**, *14*, 1217, doi:10.3390/mi14061217.
54. Gorgulu, K., Gok, A., Yilmaz, M. *et al.* All-Silicon Ultra-Broadband Infrared Light Absorbers. *Sci Rep* **6**, 38589 (2016). https://doi.org/10.1038/srep38589.
55. Oskooi, A. F.; Roundy, D.; Ibanescu, M.; Bermel, P.; Joannopoulos, J. D.; Johnson, S. G. MEEP: A Flexible Free-Software Package for Electromagnetic Simulations by the FDTD Method. Comput. Phys. Commun. 2010, 181 (3), 687–702.
56. Luan, HY., Ouyang, YH., Zhao, ZW. *et al.* Reconfigurable moiré nanolaser arrays with phase synchronization. *Nature* **624**, 282–288 (2023). https://doi.org/10.1038/s41586-023-06789-9